

Numerical simulation on the powder propellant pickup characteristics of feeding system at high pressure

Haijun Sun, Chunbo Hu^{*}, Xiaofei Zhu

School of Astronautics, Northwestern Polytechnical University, Xi'an, Shaanxi, 710072, China

ARTICLE INFO

Keywords:

Numerical simulation
Particle pickup
Two-fluid model
High pressure
Powder feeding system

ABSTRACT

A numerical study of powder propellant pickup progress at high pressure was presented in this paper by using two-fluid model with kinetic theory of granular flow in the computational fluid dynamics software package ANSYS/Fluent. Simulations were conducted to evaluate the effects of initial pressure, initial powder packing rate and mean particle diameter on the flow characteristics in terms of velocity vector distribution, granular temperature, pressure drop, particle velocity and volume. The numerical results of pressure drop were also compared with experiments to verify the TFM model. The simulated results show that the pressure drop value increases as the initial pressure increases, and the granular temperature under the conditions of different initial pressures and packing rates is almost the same in the area of throttling orifice plate. While there is an appropriate value for particle size and packing rate to form a “core-annulus” structure in powder box, and the time-averaged velocity vector distribution of solid phase is inordinate.

1. Introduction

Powder engine owns the functions of thrust regulation and multiple pulse ignitions by using metal powder as fuel and gas or solid particles as oxidant. In the early 1960s, American Bell Aerospace Company first launched the ignition validation work for aluminum powder (Al)/ammonium perchlorate (AP) powder rocket engine [1,2]. However, this project was rarely reported because it was put on hold due to limitation of powder fluidization and particle combustion technologies. As the fields of deep space detection and hypersonic flight vehicle brisking up gradually, the powder engine concept has been put forward, such as magnesium powder (Mg)/carbon dioxide (CO₂) powder engine used for Mars exploration [3–5] and the metal powder scramjet engine used for hypersonic flight vehicle [6,7]. Other work like experimental verification on powder engine has also been widely carried out [8–11].

In the process of powder engine development, powder feeding system design is always the key and difficult point for research [12]. Fricke et al. first designed a feeding system which used fluidization gas to carry powder propellant for Al/AP powder rocket [13]. And based on above idea, the relevant feeding systems were designed by a number of subsequent researchers for different types of powder engines [14–17]. In the powder pneumatic conveying system, powder packing rate should be as large as possible in order to ensure a high density specific impulse; on the other hand, the pressure in powder box should be higher than that in

chamber in order that the powder propellant can be conveyed successfully. Therefore, the pickup and fluidization process of powder propellant is a dense gas-solid two-phase flow at high pressure, which has a direct effect on the particle ignition and combustion performance. Especially in the progress of particle pickup, the characteristic of two-phase flow is quite different from that of steady conveying [18,19]. Hence, special researches need to be conducted on this.

Current researches on particle pickup properties mainly focused on the development of particle pickup velocity prediction model in atmospheric environment. And a series of semi-empirical relationships for particle pickup velocity through experiment and dimensional analysis method were built [20–22], which consist of Reynolds number, Archimedes number, grain density, particle size and other parameters. In addition, the influences of different particle types, shapes, particle sizes, and stacking forms on particles pickup property have also been studied by researchers [23–27]. While an experimental investigation on particle pickup property at high pressure was also conducted and a semi-empirical model was built for particle incipient mass flow rate [19]. In the aspects of powder fluidization at high pressure, the bubble formation and evolution mechanism are always the focuses. Researches of Kawabata et al. [28] showed that bubble rising velocity, frequency, average bubble volume fraction and the bubble merging rate would all increase as the fluidization pressure increases. Pipers et al. [29] studied the phase interactions and fluidization performance under different pressures and

* Corresponding author.

E-mail address: huchunbo@nwpu.edu.cn (C. Hu).

Nomenclature	
C_d	drag coefficient
d_s	particle diameter (m)
e	coefficient of restitution for particle collisions
g	gravitational acceleration (m/s^2)
g_0	radial distribution function
I	stress tensor
I_{2D}	the second invariant of the deviatoric stress tensor
P	pressure (N/m^2)
P_s	solids pressure (N/m^2)
R_g	gas constant [$J/(mol \cdot K)$]
T	temperature (K)
t	time (s)
\mathbf{u}_g	gas velocity (m/s)
\mathbf{u}_s	particles velocity (m/s)
Re_p	Reynolds number of particles
<i>Greek letters</i>	
β	gas/solid momentum exchange coefficient [$kg/(m^3 s)$]
γ_{Θ_s}	collisional dissipation of energy [$kg/(m^3 s)$]
ε_g	gas volume fraction
ε_s	powder volume fraction
$\varepsilon_{s,max}$	maximum packing limit of solids
Θ_s	granular temperature (m^2/s^2)
λ_g	gas bulk viscosity ($Pa \cdot s$)
λ_s	solid bulk viscosity ($Pa \cdot s$)
μ_g	gas shear viscosity ($Pa \cdot s$)
μ_s	solids effective viscosity ($Pa \cdot s$)
$\mu_{s,col}$	solids collision viscosity ($Pa \cdot s$)
$\mu_{s,fr}$	solids frictional viscosity ($Pa \cdot s$)
$\mu_{s,kin}$	solids kinetic viscosity ($Pa \cdot s$)
ρ_g	fluid density (kg/m^3)
ρ_s	solid density (kg/m^3)
τ_g	stress-strain tensor for gas phase (N/m^2)
τ_s	stress-strain tensor for solid phase (N/m^2)
ϕ	angle of internal friction ($^\circ$)

fluidization gas types, found that cracking catalyst fluidization quality improved as the velocity of fluidization gas increases, and it was greatly influenced by fluidization gas species too. Cao et al. [30] investigated experimentally on bubble size and average void rate under different pressures using the ECT technology; found that the average void rate increases with the increase of pressure, while the bubble size decreases due to the separation at high pressure.

The above researches on particles incipient fluidization characteristics are mainly by experiments, and the macro characteristics can't reveal the gas-solid two-phase flow details effectively, while numerical calculation provides a new way for studies of gas-solid two-phase flow mechanism. Currently, there are many methods can be used for gas-solid two-phase flow calculation, and the discrete element model (DEM) and two-fluid model (TFM) are both used commonly [31]. The DEM approach studies particle motion based on Lagrange coordinate system and considers the momentum transfer between particles like collision, which can obtain details of a single particle movement. In Ref. [32], the influence of fluidization pressure on bubble dynamics was researched by using DEM-CFD, and the results showed that increasing the pressure would accordingly inhibit the bubble production and stability, but would strengthen the bubbling rotation. Li et al. [33] also used the DEM method to study the flow pattern transition within the fluidized bed, found that increasing the fluidization pressure would decrease the incipient fluidization velocity and strengthen the fluidization uniformity. In addition, the particle mixing characteristics at high pressure were also studied by numerical simulation [34,35]. Results showed that increasing the fluidization pressure would reduce the number of bubble, thus increase the disorder of particle movement and enhance the mixing between particles. Meanwhile, the particle mixing time significantly shortened with the increase of the pressure. Although the DEM method can obtain the flow information of single particle and particle cloud, its simulation time is closely related with the number of particles. This method cannot be applied to calculate a large number of particles, so the above researches are all based on limited particle number, and the particle size is relatively large. While the TFM approach assumes solid phase as continuous phase like gas phase and solve the continuity equation together. This method is suitable for the numerical simulation of industrial scale dense gas-solid two-phase flow [36], whose deficiency is unable to provide single particle information.

The powder propellant incipient fluidization belongs to compressible dense gas-solid two-phase flow. Meanwhile, to improve the engine ignition and combustion performance, powder propellant mostly uses

micro particles, which leads to a huge particle number in powder box, the DEM method would have difficult in solving this problem, while the TFM approach has no limitation to the number. So this paper uses the TFM method to study the influence of pressures, particle sizes and packing rates on powder propellant pickup properties, and explores the particles pickup and fluidization law at high pressure, which will provide a good support for design of powder propellant conveying system and analysis of the engine ignition performance.

2. Experimental setup

To validate the two-fluid model, a series of experiments were performed. The experimental apparatus used in this study is illustrated in Fig. 1, which is mainly composed of gas cylinder, powder chamber, pneumatic ball valve, control computer and powder collector. A pneumatic ball valve with a response time of 50 ms is used as the switch of powder conveying. The minimum cross-sectional area of conveying pipeline is controlled by throttle orifice, and a cyclone separator is used to collect powder to prevent dust dispersion. At the beginning of experiment, put the pre-weighted powder into powder chamber, and then fill fluidized gas into it till it reaches to a certain pressure. Afterwards, open the pneumatic ball valve, the high-pressure gas in powder chamber will carry the powder through throttling orifice to the powder collector, and there will be a pressure drop in powder chamber.

The process of powder picking up is relatively short, about 1 second, so the time interval of powder entrainment was set to 1 s, which means that the pneumatic ball valve should be shut down immediately after it works for 1 s. Considering the response time of pneumatic ball valve exists in both opening stage and closing stage, the time interval would largely unaffected by response time. The pressure drop can be gained by calculating the pressure difference before and after the experiment by using pressure transducer. As a common fuel in powder engine, fine aluminum powder is used as the working medium, and inert nitrogen gas is used as fluidized gas.

3. Computational model and situations

3.1. Two-fluid model of dense gas-solid flow

The dense gas-solid flow in powder feeding system is simulated by TFM approach, and the solid phase is treated as continuous mathematically, so the generalized Navier-Stokes equations are used for the

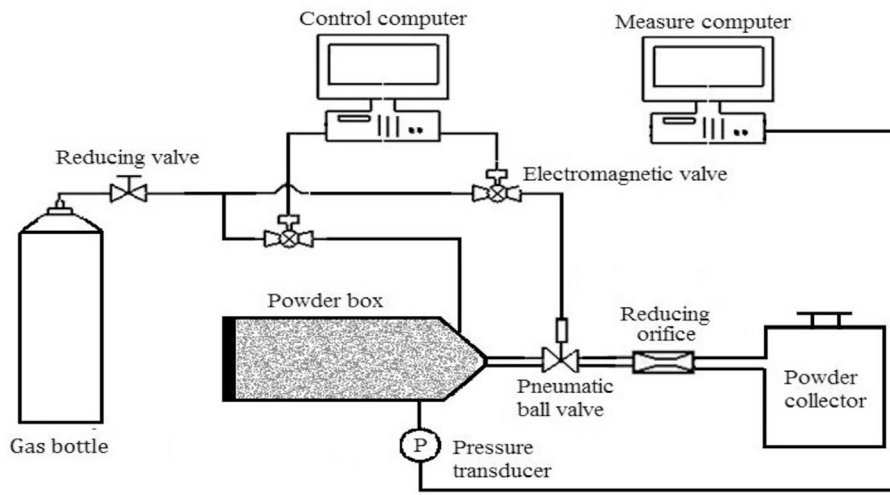


Fig. 1. Experimental system.

interaction continua. On the other hand, the constitutive relations are created to close the governing equation by using the kinetic theory of granular flows [37]. The interaction between gas and solids phases can be represented by a gas-solid drag coefficient, and many researchers concluded that the Gidaspow drag model could describe the gas-solid exchange coefficient for spouted bed reasonably [38,39], so which has been applied. The ideal gas state equation is used to describe the gas phase at high pressure for its compressibility. All the governing equations and constitutive relations for powder feeding system are shown in Table 1.

3.2. Boundary conditions and numerical solution method

The geometry of powder feeding system is shown in Fig. 2, where the scale in Fig. 2(a) is the same as the experiment in Fig. 1, the geometry was put horizontally to verify the TFM model, because it is convenient for results comparison. For powder bed, the variations of parameters in the tangential direction are negligible compared to the variations in the axial and radial directions [31], so the simplified geometry in Fig. 2 (b) has been used in this paper, and which was put erectly to compare the interaction between gravity and drag force conveniently.

The grids were built in Gambit 2.4, and the model equations given in Table 1 were solved by using the commercial CFD package ANSYS/Fluent [43]. The phase coupling of pressure-velocity was handled by “phase couple SIMPLE” algorithm, and a second order upwind scheme is used for convection terms in the momentum, turbulence and volume fraction equations. A transient simulation has been adopted, and a time step of 0.0001s with 20 iterations per time step is used to advance the solution in time.

Simulation model parameters of powder bed are summarized in Table 2, where the particle diameter, packing rate and initial pressure are the changing parameters, the aluminum with density of 2700 kg/m³ is used as particles, and the restitution coefficient is set to 0.97. At the beginning, the powder box was patched with powder and an initial pressure, and the gas phase temperature is set to 300 K.

3.3. Model verification and grid independence

To verify the TFM model for simulating the compressible dense gas-solid flow, the simulation results were compared with experiments, as shown in Fig. 3, and the pressure drop was used as comparing parameter, the pressure drop equation is list as fellow:

$$\Delta P = \frac{P_1 - P_0}{\Delta t} \quad (23)$$

where P_1 is the initial pressure and P_0 is the pressure at the end, Δt is the working time for particle pickup.

Fig. 3 shows the comparisons between the experimental and simulated pressure drops at different initial total pressure for the geometry in Fig. 2(a). There are some differences between the experimental results and simulations, which may be caused by the errors accumulation in course of simulations [44,45], but the estimates of errors accumulation can not be analyzed in this paper for the procedure codes are packaged. In general, the results comparisons are good agreements in Fig. 3, which indicates that the TFM model has the ability to simulate the compressible dense gas-solid flow to a certain degree.

In this work, the grid independence was checked with three different grid sizes for the geometry in Fig. 2 (b), and the mean particle velocity is an important parameter, which can be used to determine the sensitivity of numerical prediction to grid resolution. As shown in Fig. 4, the predicted mean particle velocity using medium grid resolution (130 × 200 × 13) is close to the velocity using finer grid resolution (150 × 250 × 15), especially in the middle area, and both of the above grid resolutions are bigger than the mean particle velocity using coarse grid (100 × 166 × 10). Hence, the medium grid resolution is used for the following simulations by considering the accuracy and computational cost.

4. Results and discussion

4.1. Flow field

Fig. 5 shows the powder volume distribution in the center section ($Z = 0$ mm) at different times. Under the interaction of drag force and gravity, powder experiences the process of pick-up first and sedimentation later. In the incipient stage (0.02s), the high pressure in powder box results in a large velocity for gas phase, so the drag force on particle is far larger than the gravity, which leads to a large number of particles being carried out. On the other hand, the bevel structure and throttle nozzle result in a sharp decrease in outlet cross-sectional area cause a limitation for particle spouting out, so the powder volume near the bevel structure increases, which would lead to powder agglomeration easily. As time goes on (0.02s-0.1s), powder located at the upper part of section is gradually carried out by gas phase. Meanwhile, it is easy to form a low volume area at the bottom of section and the area increases gradually with time. At 0.2 s, the gas velocity is lower than before, and the drag force is not large enough to overcome the gravity, so powder begins to settle, which manifests that there is no agglomeration at the bevel. Afterwards, particles gradually settle and all heap up in the bottom of

Table 1
Mathematical model.

A. Conservation laws

1) Phase mass conservation equations:

$$\frac{\partial(\varepsilon_g \rho_g)}{\partial t} + \nabla(\varepsilon_g \rho_g \mathbf{u}_g) = 0 \quad (1)$$

$$\frac{\partial(\varepsilon_s \rho_s)}{\partial t} + \nabla(\varepsilon_s \rho_s \mathbf{u}_s) = 0 \quad (2)$$

$$\varepsilon_g + \varepsilon_s = 1 \quad (3)$$

2) Momentum conservation equations:

$$\varepsilon_g \rho_g \left(\frac{\partial \mathbf{u}_g}{\partial t} + \mathbf{u}_g \nabla \mathbf{u}_g \right) = -\varepsilon_g \nabla P + \nabla \cdot \boldsymbol{\tau}_g + \beta(\mathbf{u}_s - \mathbf{u}_g) + \varepsilon_g \rho_g \mathbf{g} \quad (4)$$

$$\varepsilon_s \rho_s \left(\frac{\partial \mathbf{u}_s}{\partial t} + \mathbf{u}_s \nabla \mathbf{u}_s \right) = -\varepsilon_s \nabla P - \nabla P_s + \nabla \cdot \boldsymbol{\tau}_s + \beta(\mathbf{u}_g - \mathbf{u}_s) + \varepsilon_s \rho_s \mathbf{g} \quad (5)$$

Where

$$\boldsymbol{\tau}_g = \varepsilon_g \mu_g \left(\nabla \mathbf{u}_g + (\nabla \mathbf{u}_g)^T \right) + \varepsilon_g \left(\lambda_g - \frac{2}{3} \mu_g \right) \nabla \cdot \mathbf{u}_g \mathbf{I} \quad (6)$$

$$\boldsymbol{\tau}_s = \varepsilon_s \mu_s \left(\nabla \mathbf{u}_s + (\nabla \mathbf{u}_s)^T \right) + \varepsilon_s \left(\lambda_s - \frac{2}{3} \mu_s \right) \nabla \cdot \mathbf{u}_s \mathbf{I} \quad (7)$$

3) Granular energy equation [37]

$$\Theta_s = \frac{1}{3} \overline{u_{s,i}^2} \quad (8)$$

$$\frac{3}{2} \left[\frac{\partial}{\partial t} (\rho_s \alpha_s \Theta_s) + \nabla \cdot (\rho_s \alpha_s \mathbf{u}_s \Theta_s) \right] = (-p_s \mathbf{I} + \boldsymbol{\tau}_s) : \nabla \mathbf{u}_s + \nabla \cdot (k_{\Theta_s} \nabla \Theta_s) - \gamma_{\Theta_s} - 3\beta \Theta_s \quad (9)$$

B. Constitutive equations

1) Solid pressure:

$$p_s = \varepsilon_s \rho_s \Theta_s + 2\rho_s \Theta_s (1+e) \varepsilon_s^2 g_0 \quad (10)$$

2) Solid shear stresses

$$\mu_s = \mu_{s,col} + \mu_{s,kin} + \mu_{s,fr} \quad (11)$$

3) Solid collision viscosity [40]

$$\mu_{s,col} = \frac{4}{5} \varepsilon_s \rho_s d_p g_0 (1+e) \left(\frac{\Theta_s}{\pi} \right)^{1/2} \quad (12)$$

4) Kinetic viscosity [40]

$$\mu_{s,kin} = \frac{10 d_s \rho_s \sqrt{\Theta_s \pi}}{96(1+e) g_0} \left[1 + \frac{4}{5} g_0 \varepsilon_s (1+e) \right]^2 \quad (13)$$

5) Frictional viscosity [41]

$$\mu_{s,fr} = \frac{P_s \sin \phi}{2\sqrt{I_{2D}}} \quad (14)$$

6) Gas and solid phase bulk viscosity [42]

$$\lambda_g = 0, \quad \lambda_s = \frac{4}{3} \varepsilon_s \rho_s d_s g_0 (1+e) \left(\frac{\Theta_s}{\pi} \right)^{1/2} \quad (15)$$

7) Diffusion coefficient of granular energy [40]

$$\Gamma_{\Theta_s} = \frac{150 \rho_s d_s \sqrt{\Theta_s \pi}}{384(1+e) g_0} \left[1 + \frac{6}{5} g_0 \varepsilon_s (1+e) \right]^2 + 2\rho_s \varepsilon_s^2 d_s (1+e) g_0 \sqrt{\frac{\Theta_s}{\pi}} \quad (16)$$

(continued on next page)

Table 1 (continued)

8) Collision energy dissipation [42]

$$\gamma_{\theta_s} = \frac{12(1 - e^2)g_0}{d_s \sqrt{\pi}} \rho_s \varepsilon_s^2 \theta_s^{3/2} \quad (17)$$

9) Radial distribution function

$$g_0 = \left[1 - \left(\frac{\varepsilon_s}{\varepsilon_{s,\max}} \right)^{1/3} \right]^{-1} \quad (18)$$

10) Ideal gas state equation

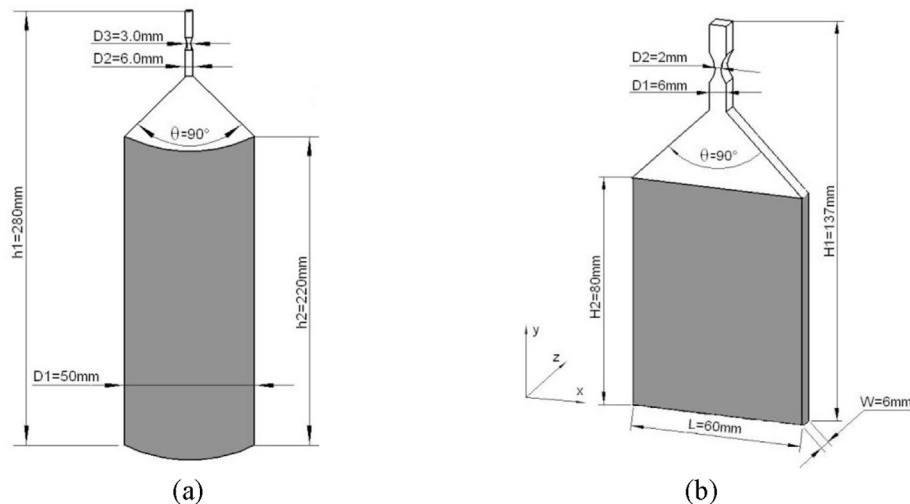
$$\rho_g = \frac{P}{R_g T} \quad (19)$$

C. Gas-solid drag coefficient [40]

$$\beta = \begin{cases} \frac{3}{4} \frac{(1 - \varepsilon_g) \varepsilon_g}{d_s} \rho_g |\mathbf{u}_g - \mathbf{u}_s| C_d \varepsilon_g^{-2.65} & \varepsilon_g > 0.8 \\ 150 \frac{(1 - \varepsilon_g)^2 \mu_g}{\varepsilon_g d_s^2} + 1.75 \frac{(1 - \varepsilon_g) \rho_g |\mathbf{u}_g - \mathbf{u}_s|}{d_s} & \varepsilon_g \leq 0.8 \end{cases} \quad (20)$$

$$C_d = \begin{cases} \frac{24}{Re_p} \left(1 + 0.15 Re_p^{0.687} \right) & Re_p < 1000 \\ 0.44 & Re_p \geq 1000 \end{cases} \quad (21)$$

$$Re_p = \frac{\varepsilon_g \rho_g |\mathbf{u}_g - \mathbf{u}_s| d_s}{\mu_g} \quad (22)$$

**Fig. 2.** Geometry of powder feeding box, (a) Experimental geometry, (b) Simplified geometry.**Table 2**
Simulation model parameters.

Description	Value
Gas density (kg/m^3)	1.225
Gas viscosity ($\text{Pa}\cdot\text{s}$)	1.82×10^{-5}
Particle density (kg/m^3)	2700
Mean particle diameter (mm)	0.02, 0.045, 0.075
Initial solids packing	0.46, 0.5, 0.55
Initial total pressure (MPa)	1, 2, 3
Restitution coefficient	0.97
Time steps (s)	0.0001
Convergence criterion	0.001
Outlet pressure (MPa)	0.101

powder box finally.

In general, the powder volume gradually increases with time in incipient stage, which shows that powder locates at different positions of powder box section is dominated by uneven force. In the upper area, the powder is mainly affected by drag force, while gravity is dominant in the bottom area, where particles settle and heap up constantly. On the other hand, in the process of powder spouting out (0.02s–0.1s), there appears a large void content near the powder box wall, which shows that it is not easy for powder agglomeration near the vertical wall, because the gas can easily form a backflow between the bevel and vertical wall.

The area-averaged axial velocity of powder at different radial sections over time is shown in Fig. 6. It can be seen that the velocity at

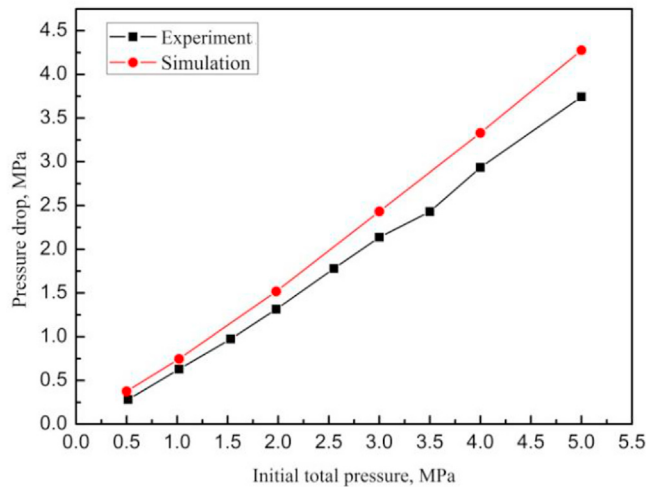


Fig. 3. Comparisons of pressure drop between experimental and numerical results.

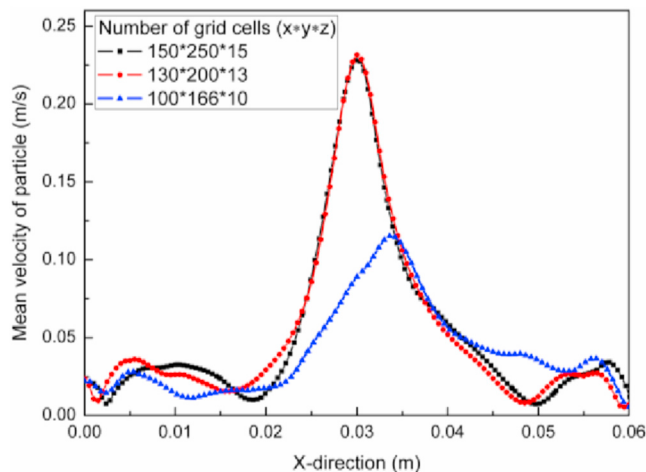


Fig. 4. Mean particle velocity for different grid resolutions.

different sections can reach the maximum at incipient stage, where the velocity of section in the upper ($y = 60$ mm) is the largest, and the smallest is in the bottom, which shows a further prove for the uneven force on powder at different positions. Along with time gone, the axial velocity shows a positive distribution first and then a negative, afterwards gradually closes to zero, that is because the powder is being picked up first and settling later. In the section of $y = 20$ mm, the axial velocity quickly changes from positive to negative, and the largest settling velocity is reached at 0.35s, then velocity gradually tends to zero. While in the sections of $y = 40$ mm and $y = 60$ mm, the velocity also has a maximum value after becoming negative., and gradually decreases and tends to zero too. Also, the velocity in middle area is larger than that in upper area during the settling process and the velocity in different sections all increases first and decreases later during this process. The reason for this might be that the powder volume fraction is large at incipient time (such as 0.2s and 0.3s), and it is easy for powder agglomeration settling, which leads to a large velocity. Then the volume gradually decreases and the agglomeration disappears, the micro-sized particles are greatly influenced by buoyancy, the settling speed decreases. While in the bottom, the settling powder gradually heap up, when the thickness reaches to 20 mm ($y = 20$ mm), powder no longer settle and the axial velocity gradually tends to zero.

4.2. Effect of pressure

The initial pressure in powder box is one of the main factors that influence the particle pickup characteristics. Fig. 7 shows the time-averaged velocity vector distribution of powder at the center section ($Z = 0$ mm) under different initial pressures. It can be seen that the vector distribution shows a basic consistent state under different pressures, the particle motion near bevel is divided into two parts: one is flowing to the outlet from two sides, the other is settling, and the settling velocity in the middle area is larger than that in the surrounding area. At the bottom of powder box, the velocity vector can easily form a “vortex” structure at low pressure (1 MPa), which tends to not obvious as the pressure increases. Meanwhile, there is an obvious dividing line of velocity vector in the section, and the altitude of dividing line represents the remaining amount of particles. Thus it can be seen that the spouting amount increases as pressure increases, which leads to the remaining amount of powder decreasing and the dividing line moving downwards. Generally, the increase of pressure leads to the vector distribution becomes more even, and a large initial pressure can effectively improve the flow distribution uniformity at the incipient stage.

In TFM approach, the granular temperature represents the turbulence intensity or pulsation strength of solid phase. Fig. 8 shows the comparison of granular temperature distribution in the middle axial line of center section ($Z = 0$ mm) under different initial pressures at 0.04s. The figure shows that there are two obvious peaks for the granular temperature distribution under different initial pressures. The first peak is at the junction of bevel and small tube, and the second is located in the throttling nozzle. The granular temperature is weakly influenced by initial pressure at an axial distance of 0–90 mm, and it increases as the pressure by enlarging the area.

Since the collision frequency will increase with powder volume, and reflect in a large granular temperature, in a sense, the granular temperature can represent the powder volume. At the first peak, the granular temperature increases as the pressure increases, that is because the flow area shrinkage leads to an agglomeration for powder, which increases the collision probability, and thus the granular temperature peak appears. While the larger pressure can make a contribution to the increase of particles velocity, thus increase its pulsation value. After the first peak, particles flow into a small diameter pipe and the volume decreases but velocity increases correspondingly, thus the granular temperature gradually decreases. When particles reach to the throttling nozzle, the narrowing change of flow section leads to particle collisions violently, that results in a sharp rise for the local granular temperature. Meanwhile, an interesting phenomenon has been found: the granular temperature distribution shows a trend of coincidence in the throttling nozzle as the pressure increases, which shows that the pressure has no influence on the granular temperature here. The above phenomenon also indicates that the powder volume in the throttling nozzle is the largest, which maintains a constant and is not influenced by the initial pressure. The phenomenon provides a good research idea for effectively revealing the mechanism of gas-solid two-phase choking flow. After the throttling nozzle, the granular temperature decreases quickly and a higher initial pressure has a larger granular temperature.

The pressure drop reflects the gas-solid two-phase flow state intuitively. Fig. 9 shows the pressure drop process in powder box under different initial pressures. It can be seen that the experimental curve has two obvious turning points, but there is only one turning point for numerical results, which corresponds to the turning point A in the experiment. Because the powder box volume in calculation is far smaller than that in experiment, which results in the pressure in small box quickly reduces to atmospheric pressure and cannot form the second turning point. By comparing the pressure drop under different initial pressures, we found that the turning points occurred at the same time almost, which shows that initial pressure has no influence on the turning of pressure drop process. On the other hand, the pressure drop time is almost the same under different initial pressures, indicates that a larger

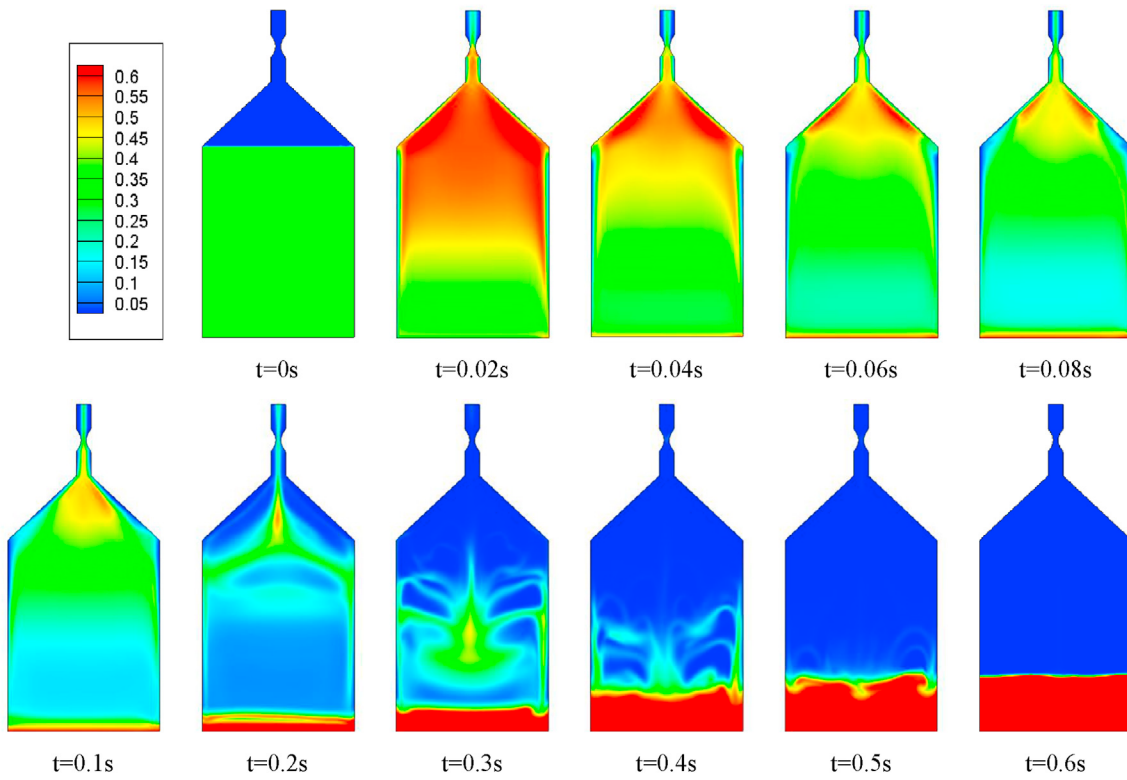


Fig. 5. Powder volume distribution at the center section of powder box with the time.

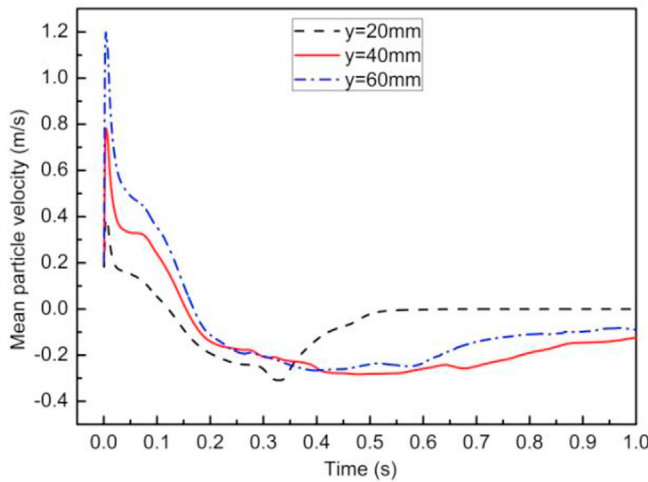


Fig. 6. Area-averaged axial velocity of particle at different radial sections over time.

initial pressure would have a large pressure drop rate.

Fig. 10 shows the area-averaged powder volume fraction over time at the section of $y = 110$ mm under different initial pressures. It can be seen that the volume fraction increases first and decreases later as time goes on. At the incipient stage, there is a peak under different initial pressures, and the smaller initial pressure, the larger peak value. Afterwards, the volume tends to be uniform since the pressure in powder box gradually tends to atmospheric pressure. Comparing Figs. 9 and 10 we can find that the pressure drop rate becomes larger when initial pressure is higher, but the volume becomes smaller instead. Because a large pressure drop rate can result in an increase of gas and solid velocity in small tube, which enables the particles quickly flowing out, so the volume is smaller under higher initial pressure.

The powder area-averaged axial velocity over time at the section of

$y = 20$ mm under different initial pressures is shown in Fig. 11. It can be seen that the particle axial velocity reaches the maximum at the incipient stage, and then decreases quickly. In the settling process, powder all reach the maximum settling velocity at a certain time under different initial pressures. Afterwards, the settling velocity gradually decreases. When the initial pressure is 1 MPa, the settling velocity is the fastest and quickly reduces to zero, but the initial pressure is large, the particle settling velocity is slow. The results mainly caused by the difference of powder accumulation degree in the bottom of powder box.

Fig. 12 shows the time-averaged particle velocity distribution at different height line of center section. At $y = 10$ mm, the fluctuation of particle lateral velocity is heavily influenced by initial pressure, and the velocity in center area is relatively larger. At $y = 30$ mm, there are obvious differences in the lateral velocity fluctuation under different initial pressures. The lateral velocity fluctuation trend is almost the same at the pressures of 1 MPa and 3 MPa, but a lower pressure would own larger fluctuation amplitude. When pressure is 2 MPa, the fluctuation form is consistent with the above-mentioned, but its peak and valley position as well as the values are different from others. At $y = 50$ mm, the lateral velocity curves are almost the same, but the velocity shows a wide distribution near the wall when the initial pressure is 1 MPa. At $y = 70$ mm, the particle lateral velocity fluctuation trend under different initial pressures is almost the same, but at 1 MPa, the lateral velocity is more large. Hence, the influences of initial pressure on particle time-averaged lateral velocity mainly focus on the middle and bottom area of powder box.

The axial velocity reflects the particle pickup state directly, as is shown in Fig. 12 (b). The distribution laws of particle time-averaged axial velocity in the upper and bottom are almost the same, where the settling velocity in center area is the largest. In the bottom section ($y = 10$ mm), a higher initial pressure would cause a larger settling velocity. While the settling velocity near the wall shows a trend of being large on the right and small on the left, which shows that the particle picking-up and settling process cannot guarantee the flow field symmetrically even in a symmetrical structure. In the middle and neither section ($y = 30$ mm and

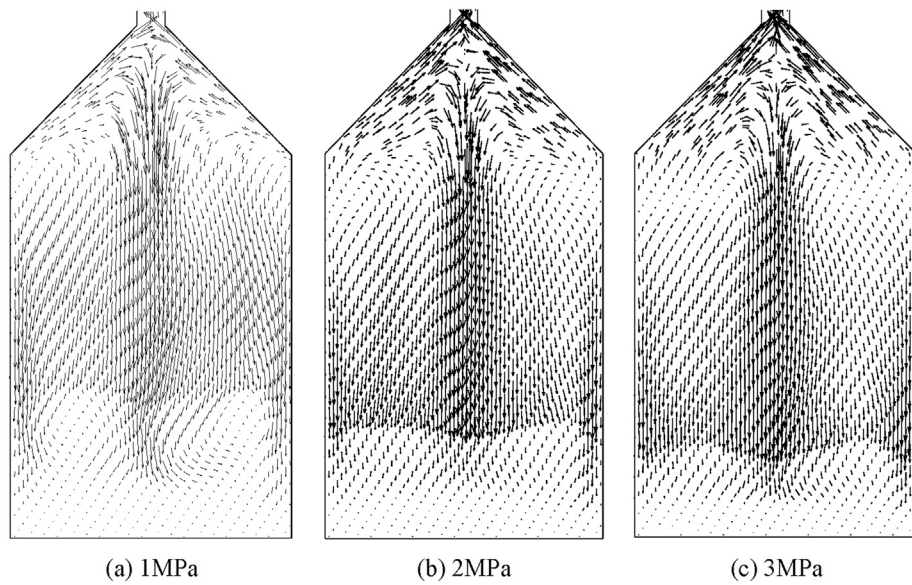


Fig. 7. Time-averaged velocity vector distribution of powder at $Z = 0$ mm section under different initial pressures.

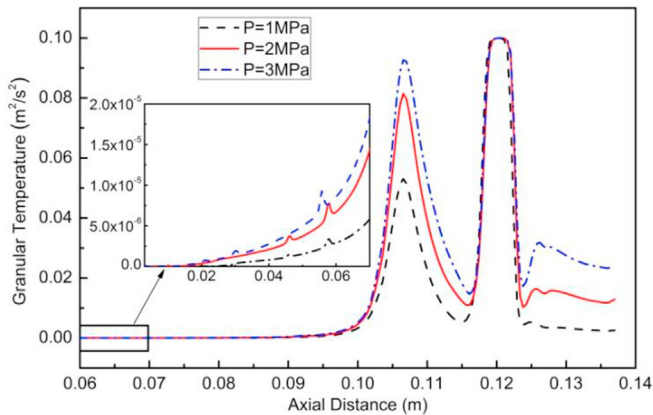


Fig. 8. Granular temperature distribution in the middle axial line of center section under different initial pressures at 0.04s.

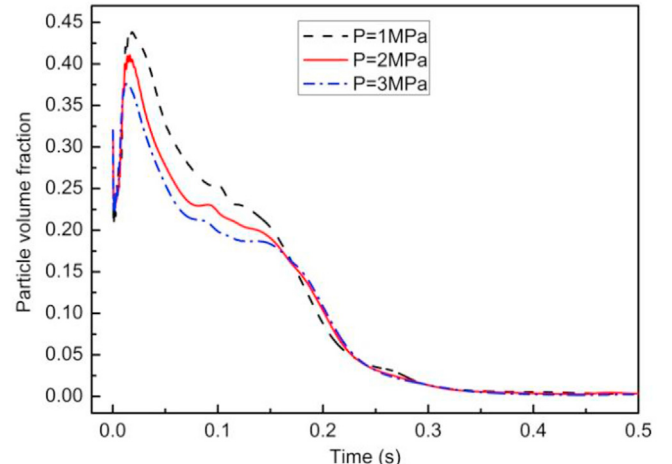


Fig. 10. Area-averaged powder volume fraction over time at the section of $y = 110$ mm.

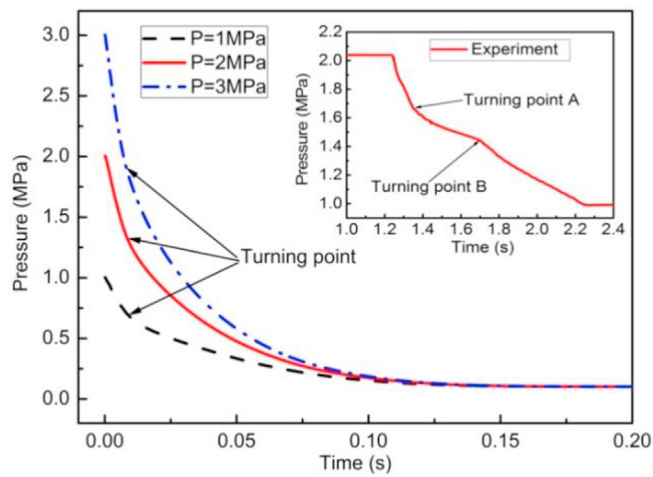


Fig. 9. Pressure drop progress under different initial pressures.

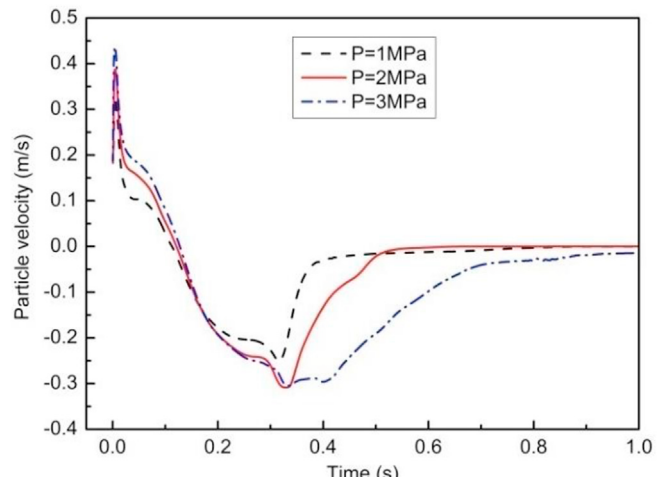


Fig. 11. Area-averaged powder volume fraction over time at the section of $y = 20$ mm

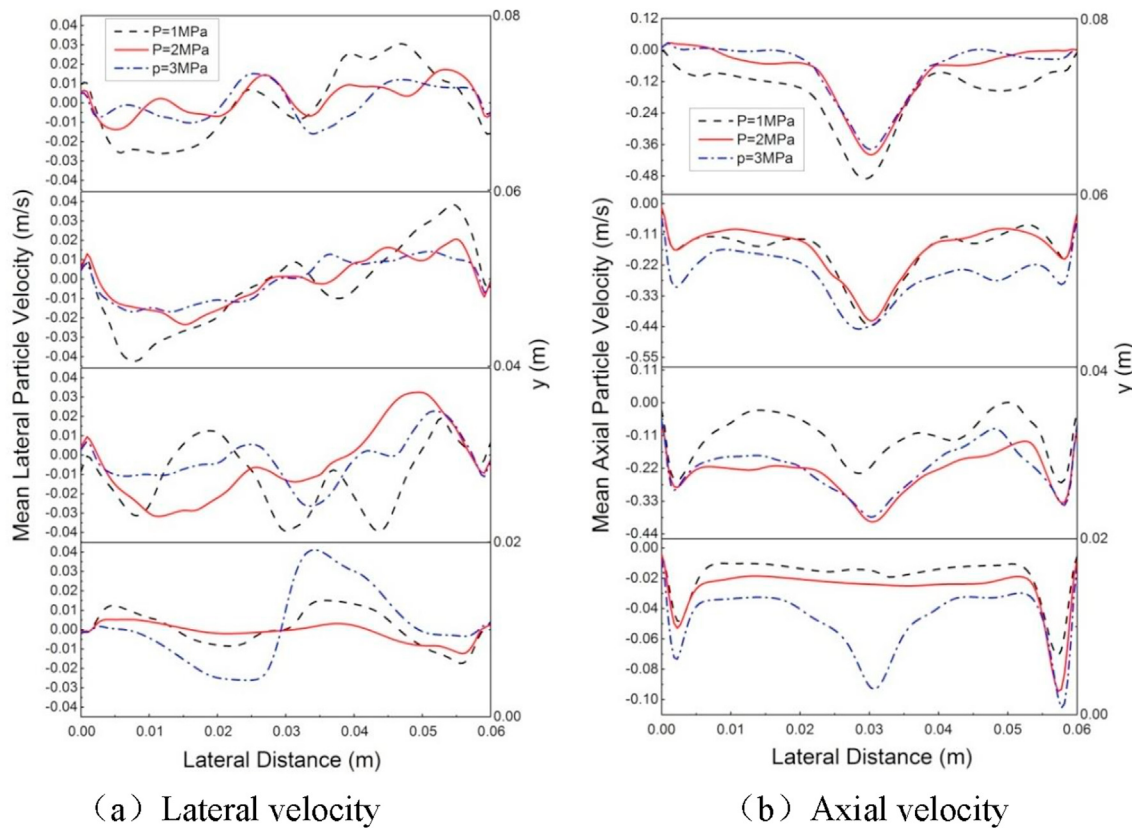


Fig. 12. Time-averaged particle velocity distribution in the center section.

$y = 50$ mm), the law is consistent with that at $y = 10$ mm while the axial velocity in the upper ($y = 70$ mm) is larger when the initial pressure is 1 MPa. Thus it can be seen that a higher initial pressure would cause a larger particle axial velocity change, which indicates that the particle would have a larger settling velocity under a higher initial pressure in the picking-up and settling process. On the other hand, the particle axial velocities are all negative, which shows that most of the time the powder is in a settling state and the picking-up process is transitory.

4.3. Effect of particle diameter

In the particle picking-up process, the dominant force on particles is heavily influenced by particle size. When particle size is small, the cohesive force among particles plays a leading role, while the gravity is the dominant force for large size particle. Fig. 13 shows the time-averaged velocity vector distribution of section ($Z = 0$ mm) under different particle sizes. When particle with a mean diameter of $20\text{ }\mu\text{m}$, the vector is upward, which shows that particles are in the picking-up state all the time. But the vector in the center area is downward while upward near the wall when particle size is $45\text{ }\mu\text{m}$, thus forming an unsymmetrical “core-annulus” structure in powder box. When the particle size is $75\text{ }\mu\text{m}$, the vector distribution is uniform, where the vector is downward near the powder box straight wall. Thus it can be seen that the particle picking-up process is heavily influenced by particle size. The gravity of a single particle is small and the gas drag force is far larger than gravity at small size, which leads to a good fluidization property, so it would be quite easy for small particles to flow out with fluid. When the particle size is large ($75\text{ }\mu\text{m}$), the gas drag force is no large enough to overcome the gravity, particles begin to settle. At middle size, there would be a harmony between gravity and drag force, which leads to the complex phenomena that contains the cases of both large and small particle sizes.

The granular temperature distribution in center axial line of section under different particle sizes at 0.04s is shown in Fig. 14. In the powder

box, the granular temperature increases with particle size, but the value is quite small. There is a granular temperature peak at the junction of bevel and small pipeline, and the peak value increases with the particle size too. In the throttling nozzle area, the granular temperatures at the particle sizes of 45 μm and 75 μm are almost the same, and that reach to the peak at the same time. When the particle size is 20 μm , the granular temperature is far lower than that of the other two particle sizes. Thus it can be seen that the granular temperature would change a lot when the particle size reduces to a certain value. In contrast, since small particle owns a good fluidization property, which can easily form a high velocity gas solid flow in a small diameter pipeline, and it is not easy for small particles to heap up in the shrinkage area. The particle volume decreases and the collision among particles becomes gentle, the granular temperature decreases. On the other hand, since the interval among small particles is larger than that among large particles, the collision probability becomes smaller than large size particle, thus small particles have a relatively lower granular temperature.

The pressure drop process under different particle sizes is shown in Fig. 15. It can be seen that the pressure drop process is almost the same and they all have a turning point, though there is a little difference in the turning time. In contrast, the pressure drop rate is larger when the particle size is larger. In general, the particle size has small influence on the pressure drop process in powder box.

Fig. 16 shows the area-averaged volume fraction over time in the section of $y = 110$ mm. It can be seen that the volume fraction of $45 \mu\text{m}$ particles is the largest before 0.3s, afterwards, the volume fraction of $45 \mu\text{m}$ particles is almost the same as that of $75 \mu\text{m}$ and the volume fraction of $20 \mu\text{m}$ particles becomes the largest at that time. Since the first 0.3s is the main picking-up period, the powder output amount is mainly decided by this period. And in **Fig. 16**, the powder output amount is the largest when particle size is $45 \mu\text{m}$, which is qualitatively consistent with the experiment result.

In order to reveal the relationship between particle size and

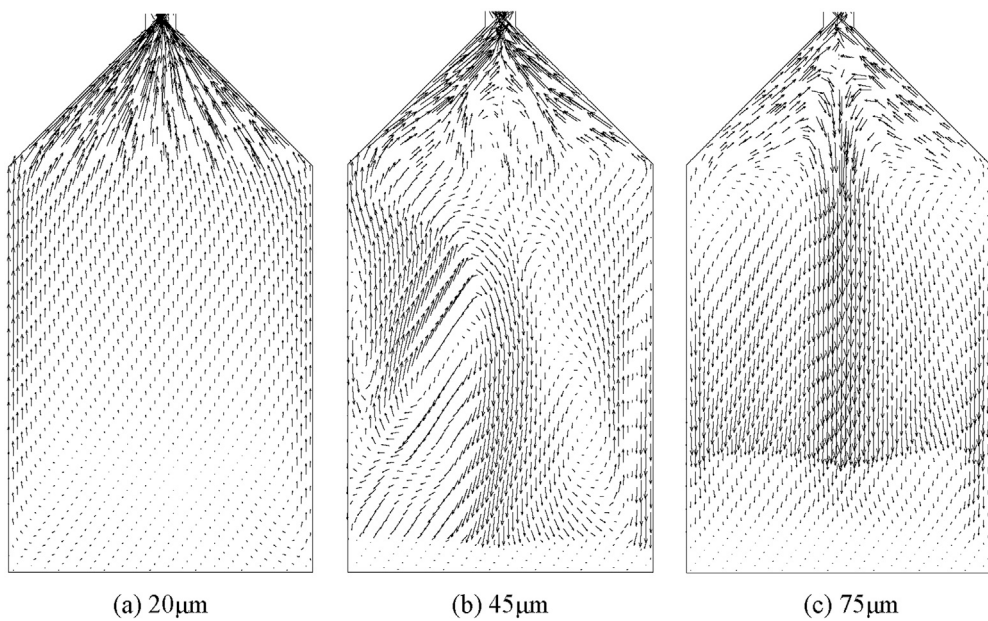


Fig. 13. Time-averaged vector distribution of powder velocity in the center section under different particle sizes.

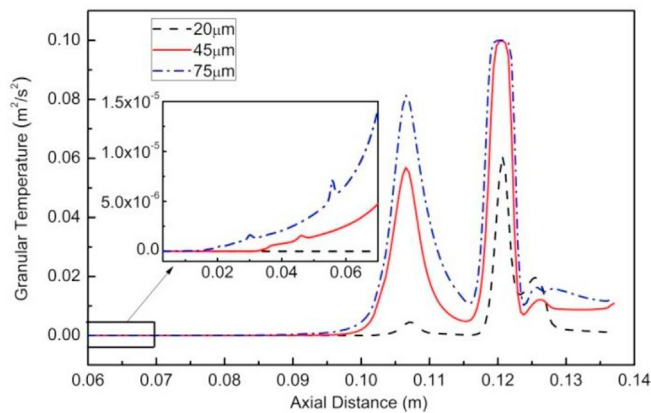


Fig. 14. Granular temperature in the axial line of center section under different particle diameters at 0.04s.

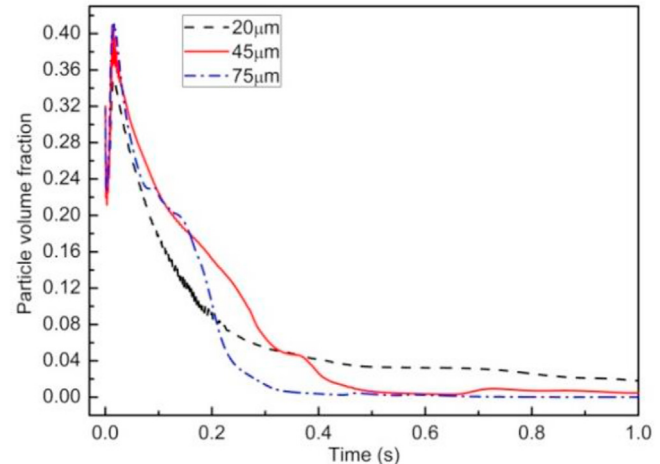


Fig. 16. Area-averaged powder volume fraction of the section at $y = 110$ mm over time under different particle diameters.

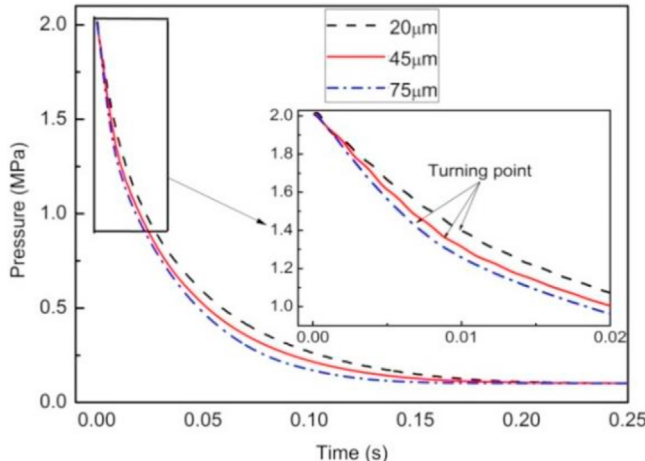


Fig. 15. Pressure drop progress under different particle diameters.

fluidization property, the average velocity of gas phase is compared with that of solid phase. Fig. 17 shows the gas and solid velocity distribution along the center axis of center section ($Z = 0$ mm) under different particle sizes. It can be seen that the gas velocity curve is close to that of solid when particle size is 20 μm , especially in the powder box, where the curves show a superposition, indicating that the powder have a good fluidization property. When the particle size is 45 μm , there is a difference between the velocities of gas and solid, and the difference is larger when it is closer to the outlet, which indicates the particle fluidization property is poor. When the particle size is 75 μm , the velocity difference between gas and solid phase increases, which shows a poorer fluidization property. This sufficiently indicates that the fluidization is stronger when the particle size is smaller in a certain size range.

4.4. Effect of powder packing rate

A higher packing rate of powder propellant would obtain a higher density specific impulse for powder engine. Under the premise that the powder can be normally fluidized and conveyed, the packing rate should

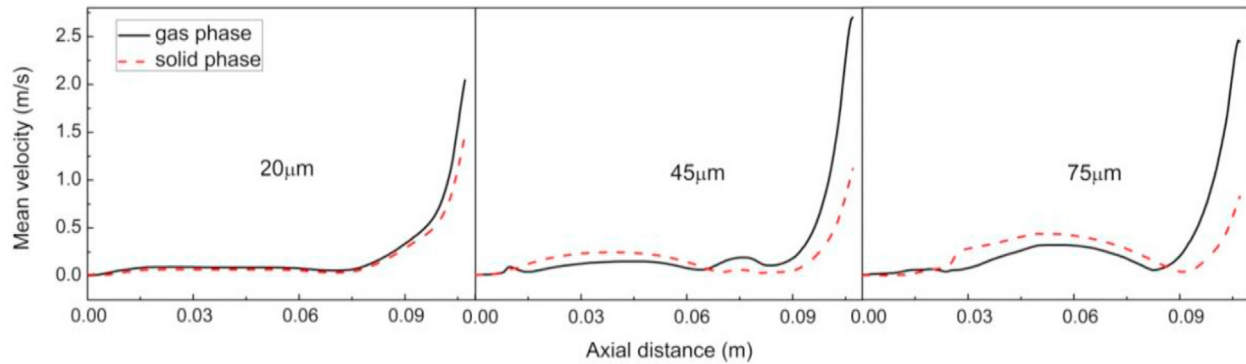


Fig. 17. Comparisons of gas and solid velocity distribution along the center axis of center section ($Z = 0$ mm).

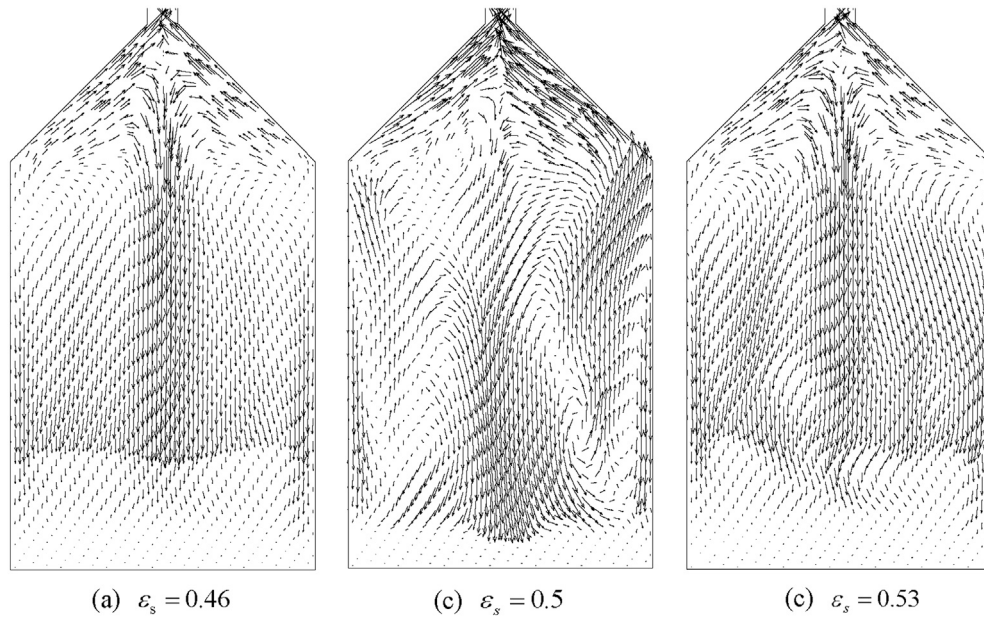


Fig. 18. Time-averaged velocity vector distribution of powder in the center section under different packing rates.

be as high as possible. Fig. 18 shows the powder time-averaged velocity vector distribution under different powder packing rates. It can be seen that the vector distribution is quite different from each other under different packing rates. When the packing rate is small, the vector distribution is uniform. As the packing rate increases ($\varepsilon_s = 0.5$), the vector

becomes inordinate and the particle flow field easily forms the “core-annulus” structure. As the packing rate goes on increasing ($\varepsilon_s = 0.53$), the “core-annulus” structure disappears and the particle flow field is consistent with that when the packing rate is 0.46, but the vector has a poor uniformity. Thus which indicates that different packing rates have heavy influence on particle flow field, and there is a certain rate which could make the velocity vector field inordinate.

Fig. 19 shows the granular temperature on the center axis of center section. Amplify the line between the distance of 0–0.06 m we can find that the granular temperature decreases first and increases later as the packing rate increases. The same law is also found at the junction of powder box bevel and small diameter pipeline. While in the throttling nozzle area, the granular temperature is almost the same under different packing rates. The peak width is larger at a higher packing rate, while the narrowest width is at the middle packing rate.

The pressure drop process under different packing rates is shown in Fig. 20. The variation trend of each pressure-time curves are almost the same. However, comparing $\varepsilon_s = 0.46$ with $\varepsilon_s = 0.53$ and we find that the pressure drop rate is smaller when the packing rate is higher. This law is qualitatively consistent with the experiments that pressure drop decreases as packing increases.

In theory, the packing rate directly influences the intervals among particles. When rate is higher, the intervals among particles are smaller, which results in a stronger viscous force among particles. Thus it would

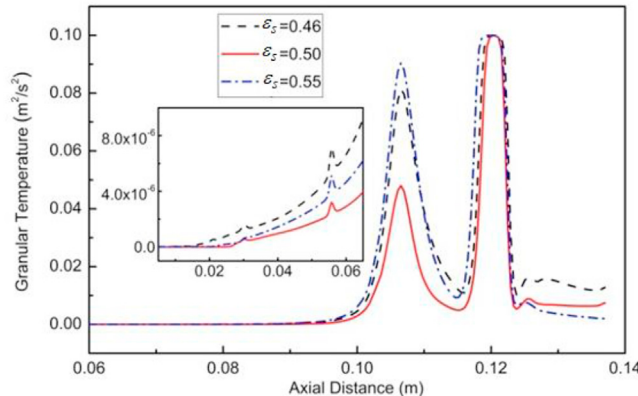


Fig. 19. Granular temperature distribution in the axial line of center section ($Z = 0$ mm) under different packing rates at 0.04s.

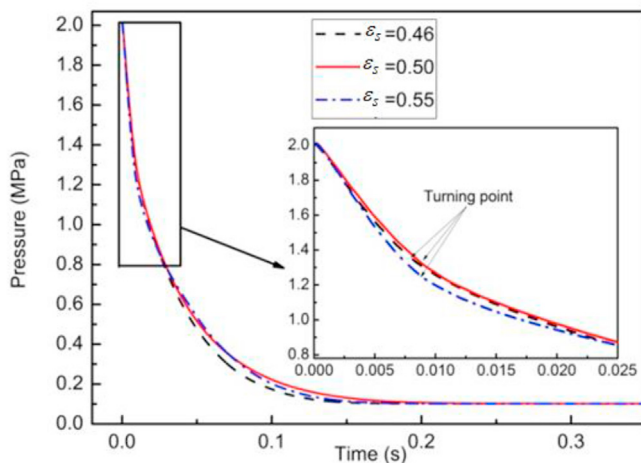


Fig. 20. Pressure drop progress under different particle diameters.

be easier for particles to agglomerate. While the gas density increases under a high pressure, which inhibits the formation of viscous force among particles. Thus there is little difference in the flow field between the low and high packing rate. When the packing rate is low, the intervals among particles are large, so the gravity plays a leading role. While the intervals among particles are quite small under a high packing rate, several small particles can be regarded as a single large particle due to the viscous force. Therefore, gravity still plays a leading role. When the packing rate is between the two cases, the gravity interacts with the drag force, which leads to large powder outlet amount; also, the flow velocity in the powder box is larger than that of the other two cases.

5. Conclusions

The TFM (Two Fluid Model) approach being applied to compressible dense gas-solid two-phase flow has been verified by comparing the simulations with the experimental results. The simulation results show that the micro-sized aluminum particles during a unit time at high pressure need to experience the pickup and settle process, and it is easy for powder to heap up near the powder box bevel segment. The initial pressure has a heavy influence on the pressure drop in powder box, and the value of pressure drop increases as the initial pressure. The distribution laws of granular temperature under different initial pressures and packing rates are almost the same at the throttling nozzle area, where the granular temperature reaches to the biggest (about $0.1\text{m}^2/\text{s}^2$). While the time-averaged velocity vector distribution of solid phase is heavily influenced by particle size and packing rate. There exists an appropriate value for particle size ($d_s = 75\mu\text{m}$) and packing rate ($\epsilon_s \geq 0.53$) to make the solid phase time-averaged vector distribution inordinate and easy to form a “core-annulus” structure in powder box.

Acknowledgements

The authors gratefully acknowledge the support from National Natural Science Foundation of China (No.51576166).

References

- [1] H.J. Loftus, L.N. Montanino, Powder Rocket Feasibility Evaluation, AIAA. 1162, 1972.
- [2] H.J. Loftus, D. Marshall, L.N. Montanino, Powder Evaluation Program, AD. 769283, 1976.
- [3] E.I. Shafirovich, A. Shiriaev, U.I. Goldshleger, Magnesium and carbon dioxide - a rocket propellant for Mars missions, J. Propuls. Power 9 (2) (1993) 197–203.
- [4] E. Shafirovich, A. Varma, Metal-CO₂ propulsion for Mars missions: current status and opportunities, J. Propuls. Power 24 (3) (2008) 385–394.
- [5] K.C. Gonyea, A.H. Auslander, R.D. Braun, Propulsion system design for a martian atmosphere-breathing supersonic retropropulsion engine, J. Propuls. Power 32 (3) (2016) 574–582.
- [6] Goroshin S, Higgins A, Kamel M. Powdered metals as fuel for hypersonic ramjets, 37th AIAA/ASME/SAE/ASEE Joint Propulsion Conference and Exhibit. 2006.
- [7] L.F. MA, Y.X. Yang, D.X. Huo, et al., Analysis on the combustion performance resulted of the big speed difference combustion stabilization device in the solid power fuel ramjet, Sci. Sin. Tech. 45 (1) (2015) 21–24.
- [8] Yao Liang, H.U. Chun-bo, et al., Firing test study on the Mg/CO₂ powdered rocket motor, J. Solid Rocket Technol. 34 (4) (2011) 440–442.
- [9] Hui-Jun Shen, Zhi-Xun XIA, et al., Experimental invest self-sustaining combustion of powdered metal fuel ramjet, J. Solid Rocket Technol. 32 (2) (2009) 145–149.
- [10] C. Li, C. Hu, X. Xin, et al., Experimental study on the operation characteristics of aluminum powder fueled ramjet, Acta Astronaut. 129 (2016) 74–81.
- [11] Y. Li, C. Hu, Z. Deng, et al., Experimental study on multiple-pulse performance characteristics of ammonium perchlorate/aluminum powder rocket motor, Acta Astronaut. 133 (2017) 455–466.
- [12] H. Sun, C. Hu, T. Zhang, et al., Experimental investigation on mass flow rate measurements and feeding characteristics of powder at high pressure, Appl. Therm. Eng. 102 (2016) 30–37.
- [13] Fricke, H. D., Burr, J. W., and Sobieniak, M. G. Fluidized Powders-A New Approach to Storable Missile Fuels, 12th JANNAF Liquid Propulsion Meeting. 1970.
- [14] J. Hu, Z. Xia, H. Shen, et al., Experimental investigation on powdered fuel ramjet combustion performance, Trans. Jpn. Soc. Aeronaut. Space Sci. 56 (6) (2013) 337–342.
- [15] Z.H.A.N.G. Sheng-min, Yang Yu-xin, HU Chun-bo. Experimental Investigation on thrust regulation of powdered rocket motor, J. Solid Rocket Technol. 3 (2015) 347–350.
- [16] T.M. Baker, T.F. Miller, Ultraviolet radiation from combustion of a dense magnesium powder flow in air, J. Thermophys. Heat Transf. 27 (1) (2012) 22–29.
- [17] D.F. Waters, C.P. Cadou, W.E. Eagle, Quantifying unmanned undersea vehicle range improvement enabled by aluminum–water power system, J. Propuls. power 29 (3) (2013) 675–685.
- [18] Szabo J, Miller T, Herr J, et al. Metal Bipropellant Rockets for Martian Ascent Vehicles, 47th AIAA/ASME/SAE/ASEE Joint Propulsion Conference & Exhibit. 2011.
- [19] Haijun Sun, Chunbo Hu, et al., Experimental investigation on incipient mass flow rate of micro aluminum powder at high pressure, Exp. Therm. Fluid Sci. 83 (2017) 231–238.
- [20] F.J. Cabrejos, G.E. Klinzing, Incipient motion of solid particles in horizontal pneumatic conveying, Powder Technol. 72 (1) (1992) 51–61.
- [21] H. Kalman, A. Satran, D. Meir, et al., Pickup (critical) velocity of particles, Powder Technol. 160 (2) (2005) 103–113.
- [22] E. Rabinovich, H. Kalman, Pickup, critical and wind threshold velocities of particles, Powder Technol. 176 (1) (2007) 9–17.
- [23] K.S. Hayden, K. Park, J.S. Curtis, Effect of particle characteristics on particle pickup velocity, Powder Technol. 131 (1) (2003) 7–14.
- [24] S.P. Goy, W.C. Jia, K. Hadinoto, Effects of binary particle size distribution on minimum pick-up velocity in pneumatic conveying, Powder Technol. 208 (1) (2011) 166–174.
- [25] J.Y.T. Tay, W.C. Jia, K. Hadinoto, Analyzing the minimum entrainment velocity of ternary particle mixtures in horizontal pneumatic transport, Ind. Eng. Chem. Res. 51 (15) (2012) 5626–5632.
- [26] L.M. Gomes, A.L.A. Mesquita, Effect of particle size and sphericity on the pickup velocity in horizontal pneumatic conveying, Chem. Eng. Sci. 104 (50) (2013) 780–789.
- [27] A. Anantharaman, A. Cahyadi, K. Hadinoto, et al., Impact of particle diameter, density and sphericity on minimum pickup velocity of binary mixtures in gas-solid pneumatic conveying, Powder Technol. 297 (2016) 311–319.
- [28] P.A. Olowson, Almsted, Influence of pressure and fluidization velocity on the bubble behaviour and gas flow distribution in a fluidized bed, Chem. Eng. Sci. 45 (7) (1990) 1733–1741.
- [29] H.W. Piepers, E.J.E. Cottaar, A.H.M. Verkooijen, et al., Effects of pressure and type of gas on particle-particle interaction and the consequences for gas-solid fluidization behavior, Powder Technol. 37 (1) (1984) 55–70.
- [30] J. Cao, Z. Cheng, Y. Fang, et al., Simulation and experimental studies on fluidization properties in a pressurized jetting fluidized bed, Powder Technol. 183 (1) (2008) 127–132.
- [31] X. Lan, C. Xu, J. Gao, et al., Influence of solid-phase wall boundary condition on CFD simulation of spouted beds, Chem. Eng. Sci. 69 (1) (2012) 419–430.
- [32] Z. Mansourpour, S. Karimi, R. Zarghami, et al., Insights in hydrodynamics of bubbling fluidized beds at elevated pressure by DEM-CFD approach, Particulology 8 (5) (2010) 407–414.
- [33] J. Li, J.A.M. Kuipers, Effect of pressure on gas–solid flow behavior in dense gas–fluidized beds: a discrete particle simulation study, Powder Technol. 127 (2) (2002) 173–184.
- [34] N.G. Deen, G. Willem, G. Sander, et al., Numerical analysis of solids mixing in pressurized fluidized beds, Ind. Eng. Chem. Res. 49 (11) (2010) 5246–5253.
- [35] Z. Amiri, S. Movahedirad, M. Shirvani, et al., The role of bubble injection characteristics at incipient fluidization condition on the mixing of particles in a gas–solid fluidized bed at high operating pressures: a CFD-DPM approach, Powder Technol. 305 (2017) 739–747.
- [36] R. Béttega, J.T. Freire, Scale-up study of spouted beds using computational fluid dynamics, Can. J. Chem. Eng. 87 (2) (2009) 193–203.
- [37] J. Ding, D. Gidaspow, A bubbling fluidization model using kinetic theory of granular flow, Aiche J. 36 (4) (1990) 523–538.

- [38] H. Lu, Y. He, W. Liu, et al., Computer simulations of gas–solid flow in spouted beds using kinetic–frictional stress model of granular flow, *Chem. Eng. Sci.* 59 (4) (2004) 865–878.
- [39] Z. Wu, A.S. Mujumdar, CFD modeling of the gas–particle flow behavior in spouted beds, *Powder Technol.* 183 (2) (2008) 260–272.
- [40] Gidaspow D, Bezburaoh R, Ding J. Hydrodynamics of circulating fluidized beds: kinetic theory approach, 7th international conference on fluidization.1991.
- [41] D.G. Schaeffer, Instability in the evolution equations describing incompressible granular flow, *J. Differ. Equat.* 66 (1) (1987) 19–50.
- [42] C.K.K. Lun, S.B. Savage, D.J. Jeffrey, et al., Kinetic theories for granular flow: inelastic particles in Couette flow and slightly inelastic particles in a general flow field, *J. Fluid Mech.* 140 (140) (1984) 223–256.
- [43] ANSYS Fluent 12.1 User Manual, ANSYS Inc., 2010.
- [44] N.N. Smirnov, V.B. Betelin, V.F. Nikitin, et al., Accumulation of errors in numerical simulations of chemically reacting gas dynamics, *Acta Astronaut.* 117 (2015) 338–355.
- [45] N.N. Smirnov, V.B. Betelin, R.M. Shagaliev, et al., Hydrogen fuel rocket engines simulation using LOGOS code, *Int. J. Hydrogen Energy* 39 (20) (2014) 10748–10756.